Promotion of Instability of a Sinusoidally Deformed Flexible Plate and its Transition to Oscillatory Motions

Diego F. Muriel[1,2,*] and Edwin A. Cowen[1,†]

[1] *DeFrees Hydraulics Laboratory, School of Civil and Environmental Engineering, Cornell University, Ithaca, New York 14853, USA*

[2] *Laboratory for Experimental Fluid Dynamics, Department of Mechanical Engineering, Johns Hopkins University, Baltimore, Maryland 21218, USA*

(Received 20 October 2019; published 27 January 2020)

We experimentally study the transition to large oscillatory motions of a thin elastic plate buckled into a second mode sinusoidal deformation. This deformation, intended to promote the onset of structural instabilities, is created by applying a permanent external net compressive force to the plate through a series of equispaced tension lines. These lines are attached to the two lateral edges of the plate, which are oriented parallel to the mean flow direction. We subject the deformed plate to an incompressible flow and find an early onset of the flutter instability (lower critical flow velocity, U_c) and increased range of periodic large oscillatory motions relative to previous studies of plates mounted in flag or inverted-flag configurations. No upstream vortex shedding or additional transversal rigidity is provided to achieve this lower U_c, which are methods used by previous researchers to initiate instability. The reduced U_c is instead achieved by the combination of three mechanisms: a deformed plate that exhibits bistability, the destabilizing action of the net compressive force on the plate, and the pressure drag on the plate existent prior to large plate oscillations. Subjected to a mean flow, U_o, the deformed plate evinces three states of motion: (a) a buckled plate with small perturbations for $U_o < U_c$ (perturbations are of the order of 0.1% of the plate's length); (b) a plate with large oscillatory motions appearing as the superposition of traveling and standing waves for $U_o > U_c$, showing fundamental oscillatory frequencies f_o, which scale with U_o, along with higher harmonics; and (c) a plate with chaotic oscillatory motions for $U_o > U_t$, a transitional flow velocity where $U_t > U_c$, characterized by a broad frequency spectrum still with a characteristic f_o, and slightly reduced relationship between U_o and f_o.

DOI: 10.1103/PhysRevApplied.13.014050

I. INTRODUCTION

Plates and membranes interacting with fluid flows are canonical problems exhibiting a broad range of physics concerning the onset of flutter instabilities. Such instabilities, which at one time were considered failure states, are now exploited for novel applications such as adaptive flow control [1,2], energy harvesting [3–10], and projectile stabilization [11,12]. Progress understanding the physics of these instabilities has been broadly useful, explaining different phenomena such as biological flows [13–18], animal locomotion [19–22], and induced vibrations in structures [23–26]. In general, the interaction of rigid or flexible plates with a flow is a problem described by the interaction between the elastic, inertial, and damping forces of the structure and the hydrodynamic forces of the fluid flow [27,28].

Efforts have been made to leverage these instabilities in the area of energy harvesting, where the basic concept is to harness the energy of the instability induced within the plates, for example, by ambient vibrations [29] or fluid forcing [3–10]. In general, conversion efficiency is paramount. When exploiting ambient vibrations, buckled configurations of plates have been used to extend the energy harvesting potential to a broader range of forcing frequencies [30–32]. In a similar manner, when exploiting fluid forcing, different geometrical configurations have been implemented to increase operational range (defined as the range of flow velocities where stable oscillations of the plate occur) and reduce the critical flow velocity, U_c, at which the flutter instability initiates [4,6–8,33–35]. Historically, Euler buckling was the first example of elastic bifurcation and instability. It involves the spontaneous breaking of symmetry at loads that exceed a critical compressive load [36]. Conversely, flapping is a dynamic instability, which can be triggered by either flutter or divergence instabilities. The former is an oscillatory vibration

*dfm99@cornell.edu
†eac20@cornell.edu

of increasing amplitude and the latter is an exponentially growing motion. Buckling occurs through divergence. A detailed treatment of instabilities is presented by Bigoni [37], whereas the behavior of rigid and flexible structures under fluid forcing, the governing equations, and the nature of the instabilities are thoroughly covered by Dowell [38, 39], Shelley and Zhang [28], Dowell and Ilgamov [40], and Paidoussis [41,42]. Here, elastic buckling instabilities are not to be confused with purely elastic instabilities occurring in viscoelastic fluids at Weissenberg numbers, Wi, of order unity and vanishingly small Reynolds numbers, Re [43].

An extensive literature on the onset of instability in plates mounted in flag or inverted-flag configurations can be found in Tang and Paidoussis [44], Eloy *et al.* [45,46], Michelin *et al.* [47], Alben and Shelley [48], Doaré *et al.* [49], Eloy *et al.* [50], Schouveiler and Eloy [51], and Fan *et al.* [52]. These works summarize and group different theoretical and numerical efforts and identify the key aspects leading to the onset of the instability. Specifically, they explore the critical velocity for the onset of the instability, the presence and breadth of the hysteresis loop on the critical velocity, confinement effects, and aspect ratio effects, amongst others. Further details on experimental and numerical studies can be grouped in the following nonexhaustive areas: the fluid-structure coupled behavior excited or forced by vortex shedding from an upstream (relative to the plate) structure [4,6,7]; the efficiency of energy extraction [5,9,10]; alternative configurations to decrease U_c [8,34,35]; the coupling in a fluid-solid-electric configuration [53–58]; periodically pitching and heaving rigid foils exploiting vortex separation [59–69]; and rigid cylinders under vortex-induced vibrations [70,71].

In terms of energy harvesting efficiency and regardless of the energy harvesting approach—the use of a mechanical coupling with an external generator [3] or the use of piezoelectric materials [72]—the fundamental goal is to achieve stable structural oscillatory motions at as low a flow velocity (i.e., as low a U_c) as possible [33,58]. For example, piezoelectric flags (canonical configuration, that is, a flexible plate tethered at its leading edge) are known to exhibit high U_c and require even higher flow velocities for consistent oscillations [4,6,33]. In addition, three-dimensional effects are known to delay the onset of instability in flag configurations [50,73]. Furthermore, alternative configurations, such as the inverted flag (i.e., a flexible plate tethered at its trailing edge), achieve oscillatory motions at lower U_c relative to the canonical configuration [33], however, at a limited operational range.

A. Our study

We investigate the interaction of a sinusoidally deformed flexible plate with a uniform turbulent incompressible mean flow (with bulk velocity U_o) and study its behavior in the presence of the plate's large oscillatory motions ($U_o > U_c$) as well as the absence of such motion ($U_o < U_c$). We demonstrate that a plate's elastic instability (buckled configuration) can be used to lower the critical flow velocity, U_c, at which flapping initiates, while simultaneously preserving or increasing its operational range. Specifically, we confirm that the sinusoidally

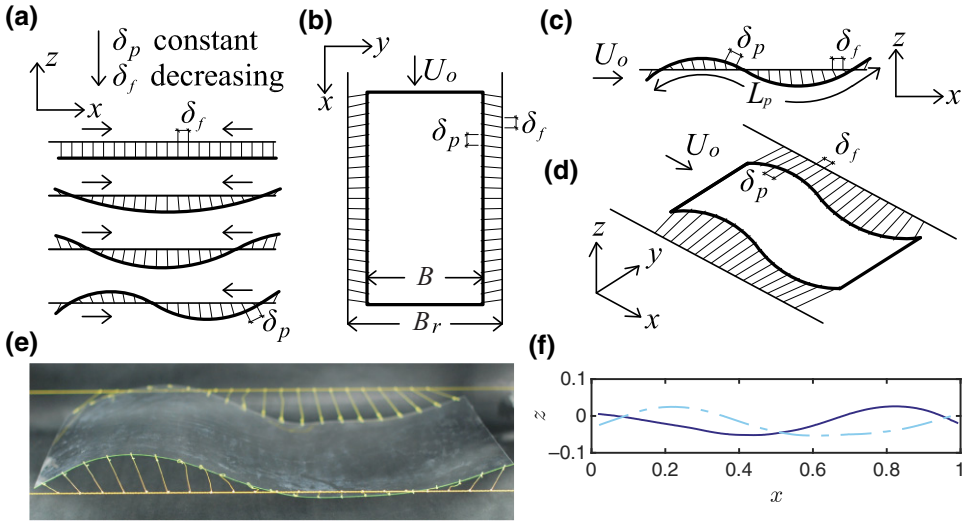

FIG. 1. Isometric representation of the deformed plate (panels (a) to (d) are adapted from Muriel *et al.* [74]). (a) Realization of sinusoidal deformation: effect of decreasing separation distance between tension line attachment points on side frame lines, δ_f, relative to a constant separation distance between tension line attachment points on the plate, δ_p, where in the topmost figure $\delta_f = \delta_p$. (b) Top view: flow velocity upstream of the prototype, U_o, plate's width, B, separation between side-frame lines, B_r. (c) Side view: plate's length, L_p. (d) Isometric projection. (e) Experimental realization of a second mode deformation. (f) Plot depicting two locally stable deformations ($x = X/L_p$ and $z = Z/L_p$).

buckled plate shown in Fig. 1 demonstrates a lower U_c and broader operational range than those found for flag or inverted-flag configurations with no need for vortex shedding from an upstream structure, a common tactic in flag- and inverted-flag-type configurations to lower U_c. The buckled configuration yields consistent oscillations at low flow velocities, allows the use of materials with higher damping modulus, and produces consistent oscillatory events at higher flow velocities, therefore achieving a broader operational range.

Herein, we present evidence of three mechanisms contributing to the onset of large oscillatory motions at low U_c: (1) the bistability of the buckled plate induced by net external compression, which forces the device into a state of permanent deformation and local equilibrium; (2) the destabilizing action of the net compressive force on the plate; and (3) the resultant unsteady flow field over the plate that induces pressure drag and lift prior to the onset of large-amplitude oscillatory motions. Moreover, we show that the deformed plate can be characterized under three states of motion: (a) a buckled plate with small perturbations at $U_o < U_c$ (perturbations of the order of 0.1% of the plate's length); (b) a plate with large oscillatory motions appearing as a superposition of traveling and standing waves for $U_o > U_c$, showing fundamental oscillatory frequencies f_o, which scale with U_o, along with higher harmonics; and (c) a plate with chaotic oscillatory motions for $U_o > U_t$, a transitional flow velocity, characterized by a broad frequency spectrum still with a characteristic f_o, and slightly reduced relationship between U_o and f_o.

II. METHODS

A. A buckled flexible plate

The plate is buckled into a sinusoidal shape by the action of equispaced tension lines [Fig. 1(a)]. We start from a flat planar state [Fig. 1(a), top] and increase the net compression force to our plate by decreasing the attachment point separation distance on the frame, δ_f. When this net compression exceeds Euler's critical load, large deflections appear, first, as a mode 1 deformation and, then, as a mode 2 deformation [Fig. 1(a), bottom]. A mathematical model of the described deformation is presented by Muriel and Cowen [75].

The plate is made of a single translucent polycarbonate sheet with thickness $\delta = 0.400$ mm, length $L_p = 60$ cm, width $B = 30$ cm, density $\rho_p = 1.14$ g/cm^3, water absorption 0.15%–0.34%, and tensile modulus $E = 1.97$ GPa. The applied net compression force is created using inner tension lines mounted to parallel side-frame lines. The side-frame lines are made of a 0.4 mm diameter microfilament braided line (Spectra®) rated to 471 N. Similarly, the tension lines are composed of a microfilament with length $L_s = 7.6$ cm, separation distance along the plate of $\delta_p = 2.90$ cm and separation distance along the side frame of $\delta_f = 2.45$ cm. This difference between the two separation distances (δ_p and δ_f) provides the external compression force necessary to induce the plate's deformation, with maximum achievable deformation height of 28.9 mm ($\sim 0.05 L_p$, crest to trough). The entire device is mounted within a frame made of extruded aluminum alloy, which sets the separation between side-frame lines to $B_r = 44.10$ cm, and positions the plate 15.0 cm above the bottom of a recirculating-type open-channel flume.

B. Nondimensional parameters

We define

$$\mathrm{Re} = \rho_f U_o L_p/\mu, \tag{1a}$$

$$u_o = U_o\sqrt{\rho_f B L_p^3/D}, \tag{1b}$$

$$r = \rho_p \delta/\rho_f L_p, \tag{1c}$$

$$m_a = M_a/\rho_f L_p, \tag{1d}$$

$$\beta = D/\rho_f U_o^2 L_P^3, \tag{1e}$$

$$\text{and } p^* = P/\rho_f U_o^2 L_P, \tag{1f}$$

where Eq. (1a) is the Reynolds' number based on the length of the plate, Eq. (1b) is the reduced velocity, Eq. (1c) is the dimensionless mass ratio, Eq. (1d) is the dimensionless added mass, Eq. (1e) is the dimensionless bending stiffness, and Eq. (1f) is the dimensionless compression force. Here, ρ_f represents the density of the fluid, U_o the upstream bulk velocity, μ the dynamic viscosity of the fluid, D the flexural rigidity defined as $D = EI/(1-\nu^2)$, with E being the Young's modulus, I the area moment of inertia, and ν Poisson's ratio [76], M_a the dimensional added mass, and P the dimensional compression force.

We maintain material and geometric properties across all experiments and vary u_o and Re from 9.2 and 4.1×10^4 up to 82.2 and 3.7×10^5, respectively. Here r is equal to 7.6×10^{-4}, β varies from 3.6×10^{-3} to 4.4×10^{-5} from lowest to highest flow velocity with fixed D, and p^* varies from 4.4×10^{-1} to 5.4×10^{-3} from lowest to highest flow velocity with fixed P. The dimensionless form of the critical (u_c), bulk (u_o), and transitional (u_t) velocities will be used from now on. Note that the specific u_o where oscillatory motions first occur is by definition u_c.

C. Experimental facility

Experiments are conducted in an 8.0 m long, 0.60 m wide recirculating-type open-channel flume with glass sidewalls and super abrasion resistant (SAR) acrylic bed in the DeFrees Hydraulics Laboratory in the School of Civil and Environmental Engineering at Cornell University. Two variable frequency controlled centrifugal pumps drive a constant water depth across all experiments of $h =$

37.0 cm [$h = 35.0$ cm for particle image velocimetry (PIV) measurements]. The bed slope is set at 0.0 (i.e., horizontal), with negligible streamwise acceleration [$\partial U_b^2/\partial x \sim 0$ to experimental uncertainty, with the depth-averaged mean velocity at the centerline of the flume defined as $U_b \equiv (1/h)\int_0^h U(z)\,dz$]. A turbulent boundary layer is tripped by a 4 mm tall rectangular steel bar mounted on the bed in the transverse direction and located at the entrance of the flume test section, downstream of inlet conditioning screens. A 15 μm porous felt is used to filter suspended particles of diameter greater than that of the felt. The coordinate system is defined with x in the streamwise direction, z as the vertical distance from the bed to the water surface (positive upwards), and the y direction is set by the right-hand rule.

D. Experimental study cases and techniques

Three distinct datasets are collected. First, acoustic Doppler velocimetry (ADV; Nortek Vectrino equipped with + firmware) measurements are used to determine the onset of large oscillatory motions and to characterize the evolution of the plate's oscillatory frequency, f_o, as a function of u_o. Second, imaged-based edge detection is used to characterize the plate's large oscillatory motions, including their wave composition and frequency, again as a function of u_o. Third, PIV measurements are made, which are then used to calculate the pressure fields and forces acting on the plate. To obtain time-averaged pressure fields, we assume the time-averaged flow field to be two dimensional and integrate the Reynolds-averaged momentum equation [77,78]. A detailed summary of the study cases using ADV, image-based point detection, image-based edge detection, and PIV can be found in Appendix A. Details on uncertainty analysis can be found in Appendix B.

1. Particle image velocimetry

The flow velocity in the vicinity of the model is measured with PIV. Digital images are collected with two Andor Zyla 5.5 MP sCMOS cameras (2160 × 2560 pixels, 16 bits per pixel, run at 20 frames per second, yielding 10 Hz velocity fields) equipped with 50 mm Nikkor lenses. The image area is illuminated with a Spectra Physics PIV 200-10 Nd:YAG laser (200 mJ/pulse at 532 nm, 10 Hz dual head). A laser light sheet is formed using a cylindrical lens ($f = -6.4$ mm) and the beam is focused with one spherical lens ($f = 1500$ mm) to provide a maximum light sheet thickness of 1 mm over the field of view. This configuration provides a resolution of 144 μm/pixel covering an area of 31.1 cm × 73.7 cm. Upstream bulk velocity is measured with a single ADV with its measurement volume located $5L_p$ upstream from the leading edge of the plate and 15.0 cm above the bed (i.e., at the mean elevation of the plate), with a sampling frequency of $f_s = 200$ Hz.

A Berkeley Nucleonics Inc. (San Rafael, Calif.) BNC500A digital delay generator is used to trigger the flash lamps and Q switches on the Nd:YAG laser system with temporal delay between image pair illuminations, Δt, chosen to limit the maximum particle motion within an image pair to ∼10 pixels, allowing a final PIV subwindow of 32 × 32 pixels to be used to determine the displacement field. The flume is filled with water to the desired depth and seeded with Sphericel particles (hollow glass spheres, mean density 1.1 g/ml, median diameter 11.7 μm, manufactured by Potters Industries, Inc., Valley Forge, Pa.).

Prior to cross-correlation analysis, an intensity-count-based digital mask is used to reduce the influence of the highly reflective plate. We do not conduct a correlation-tracking-based mask technique [79]; instead, after the mean velocity field is subtracted from each image, pixels inside the digital mask are set to zero.

Image pairs in the x–z plane are analyzed with the dynamic subwindow PIV scheme described by Cowen and Monismith [80] and extended to second-order accurate based on Wereley and Meinhart [81]. A total of 4250 image pairs at 5 Hz are analyzed for cases at $u_o < u_c$. The analysis comprises an iterative scheme with 5 displacement estimate passes, with the final pass utilizing 50% overlapped 32 × 32 pixel subwindows, yielding a grid resolution of approximately 2.3 mm vertically and horizontally, resulting typically in 20 724 analyzed subwindows per image pair. The full field of view is composed of two of these independent data fields (i.e., two cameras, each recording half of the field of view), forming a grid of 132 × 314 vectors in the vertical and horizontal axes, respectively.

III. RESULTS AND ANALYSIS

A. The transition to large oscillatory motions

Our results show that large structural oscillations are initiated at $u_c = 25.7$ (Fig. 2). The limits of the hysteresis loop, where u_c differs if it is found by decreasing or increasing u_o, are small and are determined to be $\pm 0.02u_c$. We test this same plate (i.e., material, thickness, and aspect ratio), in a flag configuration, that is, with only a tethered leading edge. This test yields weak perturbations up to $u_o = 28.1$ (amplitude of the perturbations are smaller than the order of 0.1% of the plate's length), small amplitude and intermittent oscillatory motions up to $u_o = 61.2$ (hovering), and shows no evidence of a developed flutter instability up to $u_o = 94.5$, where our facility reaches its maximum u_o. The observed perturbations at these velocity ranges for our flag type configuration tests are attributed to surface and three-dimensional effects (see Supplemental Material for video *VFlagType.mp4* of the tethered leading edge configuration at $u_o = 94.5$ [82]).

As a comparison, Shelley *et al.* [83] studied a flag-type configuration that remained flat even at speeds as

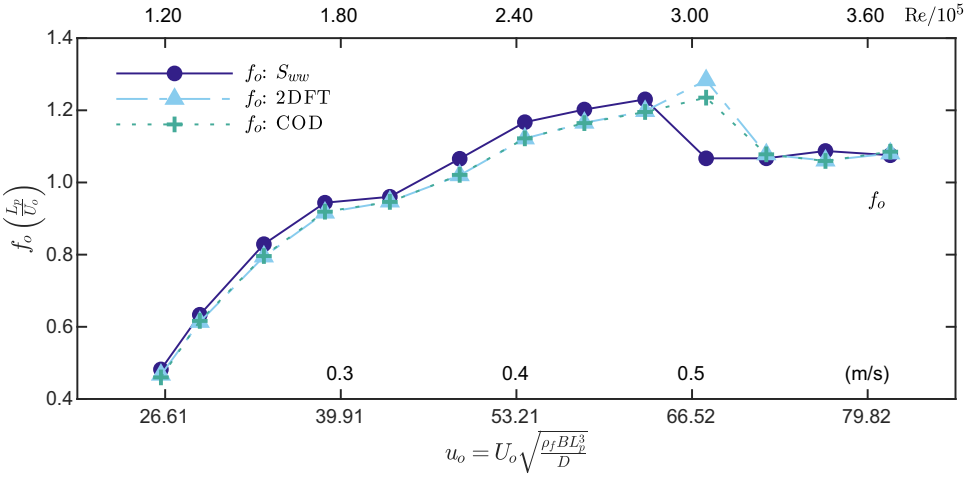

FIG. 2. (a) Evolution of oscillatory frequency, f_o, as a function of flow velocity, u_o. Results are for f_o through spectral analysis of velocity measurements of a fluid parcel, S_{ww}, and through two-dimensional Fourier transform (2DFT) and complex orthogonal decomposition (COD) of the plate's image-based-detected edge.

high as $U_o = 0.90$ m/s, which can be rendered dimensionless using their material properties, corresponding to $u_o = 4.2 \times 10^4$. As they discussed, the absence of instability at such a high flow velocity is due to the inability of the flag's inertial forces to overcome the fluid's stabilizing forces (drag). In an effort to incite instability, Shelley *et al.* [83] used copper strips to add lateral stiffness and achieved transition to a flapping state at $U_c = 0.81$ m/s ($u_c = 197.0$). Three-dimensional effects at $u_o < u_c$ are prevented in our study by the action of the tension lines, which do not add inertia to the system. An additional study on heavy flags reported a critical velocity of $U_c = 0.57$ m/s [9], which in dimensionless form is $u_c = 76.2$. Additional stiffness to this system is provided by ionic copolymers attached to the surface of a flexible mylar sheet, resulting in a lower u_c than that of Shelley *et al.* [83].

Care must be taken when exploring such differences in u_c for different configurations. For example, in the presence of a buckled plate (i.e., this study), an unsteady flow field is present before oscillations start. In contrast, on a flat plate the evolution of oscillatory motions is coupled to the evolution of the unsteady hydrodynamic forces. We therefore demonstrate an alternative configuration to achieve the transition of a flexible plate to a flapping state, where a dominant pressure drag overcomes the stabilizing forces of the system, therefore reducing u_c compared with that expected for flag-type configurations. In the following sections we present the main mechanisms for this reduction.

B. Mechanism one: bistable systems

A system that exhibits two stable equilibrium states, known as a bistable system, can be described by a unique double-well restoring force potential [29]. Through stable state switching, these systems transition from one stable state to the other, causing large-amplitude motion. It has been demonstrated that bistable energy harvesters are an improvement upon their linear counterparts operating in their steady-state vibrational environments. In addition, they have been analytically and experimentally shown to provide as much as an order of magnitude more harvested energy [29–32,84].

To achieve a bistable system and reduce the requisite dynamic external loading (i.e., fluid forcing) necessary to induce large oscillatory motions on our plate, we provide a net external compressive force and create the well-known buckling instability. The second mode deformation, seen in Fig. 1(e), is stabilized through the action of external constraints (i.e., tension lines). Our plate, which by design is free to move, provides no opportunity to apply moments or internal forces at the boundaries. Therefore, the plate requires the action of the tension lines to stabilize the sinusoidal deformation and create the bistable system.

The solution to the nonlinear system of equations describing the plate's shape shows more than one possible structural deformation for a single external compressive force [see Figs. 1(d)–1(f), and Muriel and Cowen [75]]. This is evidence of the instability (i.e., buckling) and corroborates the formation of a bistable system. More importantly, the action of any additional external force, either numerically or experimentally, will induce intrawell oscillatory motions or large motions, to be described in the following sections.

C. Mechanism two: external compression

It has been demonstrated by Dowell that the flutter-type instability is aggravated by a compressive in-plane load for double-pinned plates [85–88] and for double-pinned cylinders by Paidoussis [89]. Following Connell and Yue [90], a flat plate under compression is described by

$$(r + m_a)\frac{\partial^2 z}{\partial t^2} + \left(p^* - 1.3\mathrm{Re}^{-1/2} + m_a\right)\frac{\partial^2 z}{\partial x^2} + \beta\frac{\partial^4 z}{\partial x^4} + 2m_a\frac{\partial^2 z}{\partial x \partial t} = 0, \tag{2}$$

where each of the terms in Eq. (2) correspond to the plate's inertia, added mass inertial effects, compression, fluid-induced tension, Coriolis force, bending stiffness, and centrifugal force, respectively. With a subsequently derived dispersion relation, it can be demonstrated that bending rigidity, fluid-induced tension, and the Coriolis force are stabilizing, whereas external compression and centrifugal forces are destabilizing [77,87,89,90].

From the above it is clear that compression has a destabilizing effect in our system and as the net compressive force increases, the point at which the instability occurs (i.e., u_c) decreases. Nevertheless, to create the sinusoidal deformation, the system must overcome the critical Euler load and enter a buckling state. In this state, the linear equations describing the plate become invalid. Once flow separation occurs owing to the induced curvature on the plate, the fluid coupling becomes invalid as well. Instead of pursuing further the development of a more complex analytical or computational model, we approach the problem from an experimental perspective to describe the kinematics and dynamics of the plate and to study the hydrodynamics of the fully coupled fluid-structure interaction problem.

We note that the effects of increasing net compressive loads on the requisite bulk velocity for onset of the instability, namely u_c, are not tested in this study. Muriel and Cowen [75] studied the effects on deformation as compression was progressively increased, but the effect of this progressive increment on u_c is left for future studies.

D. Mechanism three: unsteady flow field prior to the onset of large-amplitude oscillatory motions

1. The presence of small perturbations

Our experiments reveal small-amplitude displacements in the plate for $u_o < u_c$ (see Fig. 3 and the accompanying video *Fig3.mp4* in the Supplemental Material [82]). The unsteady fluid forces that result from the interaction of the flow with the sinusoidally deformed plate force the plate to continually reconfigure. This is a response to the dynamic forces and occurs without the plate transitioning into large oscillatory motions. This behavior is possible not only due to the action of the unsteady fluid forces, but also because the deformation of the plate is bistable. Large turbulent fluid ejection events can be seen in Figs. 3(a)–3(e), where the plate's location provided in each frame is its mean position and the instantaneous plate location can be identified from the high-vorticity streak close to plate's mean position. In addition, it can be seen how vorticity is formed at the concave face behind the plate's leading edge, diffused by the action of the boundary layer, advected away from the plate by virtue of flow separation, and advected downstream by the mean flow.

As u_o increases, the frequency of advected vorticity events increases. The dynamic pressure inside these vortices is lowest in the core region, which creates suction events, causing the small-amplitude oscillations [see Fig. 3(f)]. Such small-amplitude oscillatory motions grow progressively, aided by the progressive change in applied fluid forces, which in turn induce large oscillatory motions as flow speed increases (see Supplemental Material for video *Fig3Inverted.mp4* depicting an additional example of unsteady flow field at $u_o = 16.9$ [82]). While unsteady fluid forces have been used effectively on rigid foils [59–69], here we present evidence of how unsteady flow fields can be used on bistable systems.

2. Plate reconfiguration under unsteady flow field

Our results show that under fluid forcing the plate adapts its shape as the mean force increases with u_o. This is further evidence of the bistability of the plate, where now a reconfiguration of the structure is caused by the external load provided by the mean flow field. Without transitioning to large oscillatory motions, the second mode deformation is preserved, whereas the maximum and minimum curvature points, as well as the zero curvature points, are all displaced downstream [see Figs. 4(a) and 4(b), where positive and negative refer to the curvature's sign at the plate's leading edge]. This is a direct response to the mean fluid forces applied to the plate, where at higher flow speeds, new equilibrium positions are required to balance the forces on the compliant plate. Limits to this deformable behavior are established by the boundary conditions induced by the tension lines. They restrict the range of motion of certain plate locations (connection between plate and tension line) to an area rather than a fixed point in space. For example, although tension lines are active at the leading and trailing edges, they are slack in the midspan, allowing for reconfiguration (i.e., additional equilibrium positions).

It should be noted that we present four cases for the negative phase [Fig. 4(a)], whereas we present five cases for the positive phase [one additional case for u_o close to, but just below u_c, Fig. 4(b)]. This is due to the fact that at $u_o = 19.5$ (i.e., $\mathrm{Re} = 0.92 \times 10^5$, the fifth and highest flow speed presented for the positive phase), when we start the deformation in a negative phase, the plate *snaps through* (where a point of maximum curvature rapidly transitions to a point of minimum curvature and vice versa, a form of dynamic mode branching) into the positive phase and acquires an equilibrium position without transitioning to large oscillatory motions. Such behavior is likely explained by the geometric asymmetry of the configuration, having the influence of a bottom boundary layer (i.e., flume's bottom) on one side and a free surface on the other.

Turning our attention to the characteristics of the flow, we can see how an irrotational description of the problem is not appropriate [Figs. 4(c), 4(d), and 4(g)]. The dimensionless mean vorticity fields show vorticity diffused from

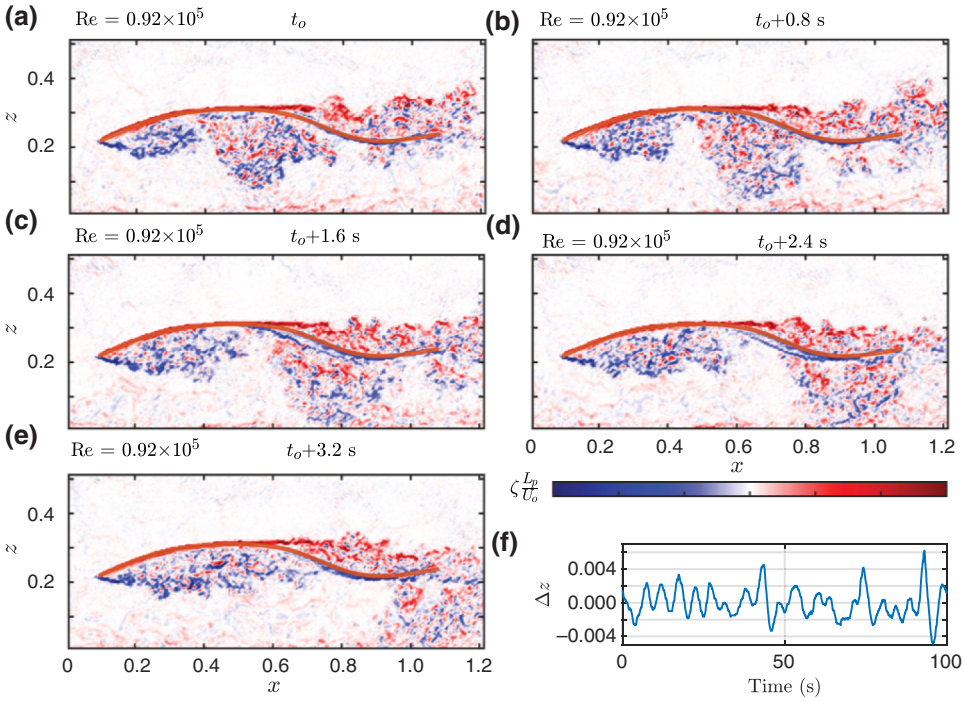

FIG. 3. (a)–(e) Unsteady flow fields for u_o just less than u_c. The dimensionless vorticity fields are depicted for $u_o = 19.5$ (Re = 0.92×10^5), which is the highest upstream bulk velocity tested that is less than u_c. Mean plate location is depicted in orange. (f) Dimensionless small-amplitude perturbations, Δz, for the same case.

the plate's boundary layers into the concave face region behind the plate's leading edge, as well as into the concave face region on and after the first location of zero curvature. In a linear sense, this position marks one quarter of a wavelength of the sinusoidal deformation if we linearize the geometric description.

High-vorticity events are present, particularly behind the leading edge, at the first location of zero curvature, as well as in the boundary layer around the plate, where the no-slip boundary condition must hold. The separation phenomena is a well-studied and prolific area of research and a nonexhaustive literature review reveals studies of turbulent flow over curved surfaces [91–107], turbulent flow over a curved hill [108–111], turbulent flow over fixed wavy surfaces [112–118], turbulent flow over progressive surface waves and compressible flow [119], turbulent flow over flexible cambered plates [120–127], and turbulent flow over a body undergoing streamwise motion [128].

As the plate's sinusoidal deformation is always present, the existence of unfavorable pressure gradients force the flow to separate even at the lowest flow velocities studied ($u_o < u_c$). Unfavorable pressure gradients force the viscous boundary layer to separate, whereas favorable pressure gradients make the boundary layer more robust to separation. Both effects are present in our flow. The effect of the pressure gradients can be seen in the recirculation zones depicted by the streamlines in Figs. 4(e) and 4(f) and the boundary layer separation depicted in Fig. 4(g) [see Supplemental Material for the corresponding videos of Figs. 4(e) and 4(f) [82]]. A common characteristic across all test cases is that the flow downstream of the separation point is often unsteady and chaotic, resulting in a dominant pressure drag (form drag), which is a fundamental mechanism for the low u_c.

3. Mean pressure fields, mean forces on the plate, and their influence on plate deformation and transition to large oscillatory motions

Mean pressure fields corroborate the presence of favorable and unfavorable pressure gradients, which contribute to the existence of flow separation, recirculation zones, and reattachment [Figs. 5(a) and 5(b)]. In Figs. 5(c) and 5(d) we see that drag increases with flow velocity and lift exhibits a decrease (increase) in its magnitude for the positive (negative) phase as it approaches u_c. As the deformation is bistable, these changes indicate the limits where a reconfiguration will be necessary to maintain equilibrium. As further deformations of the plate are not possible (i.e., the crest of the positive phase or the trough of the negative phase cannot be deformed indefinitely owing to the finite length tension lines), the change in forces cannot be sustained under the same phase of deformation. Physically, the increase in u_o progressively deforms the plate and as boundary conditions restrict the deformation (i.e., tension lines), there is a flow regime where equilibrium will not be achieved owing to such restrictions, inducing either a phase change (snap through) or large oscillatory motions.

E. States of motion

Our study reveals three states of motion based on the relationship between the plate's fundamental oscillatory

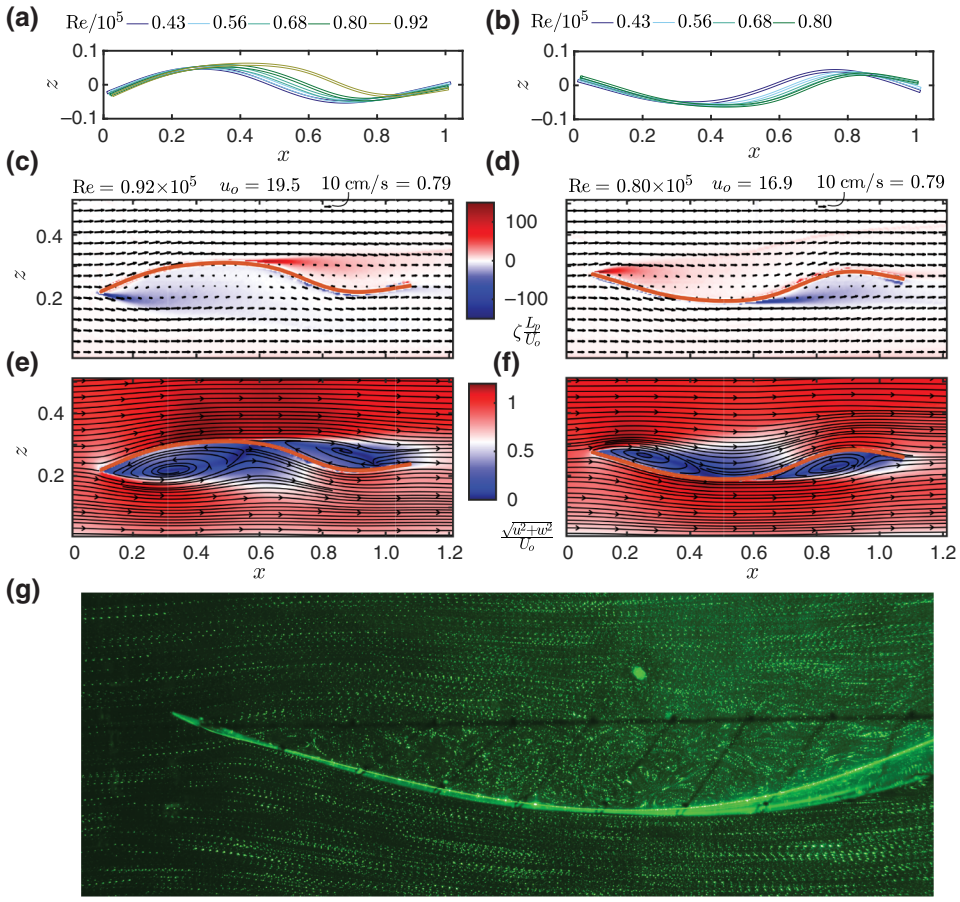

FIG. 4. Shape adaptability as a function of flow speed for the positive (a) and negative (b) phases at $u_o < u_c$. The plate's deformations are extracted from the first image of the PIV pair and represent the average location of the plate during the test under study. (c),(d) Dimensionless vorticity fields ($\zeta L_p/U_o$, where ζ is vorticity); the vectors represent the velocity fields. (e) Boundary layer separation: the image contains 10 laser exposures of the immersed plate in a fluid with suspended particles.

frequency, f_o, its oscillatory frequency harmonics, and u_o. As described previously, at $u_o < u_c$, the induced buckled state is well represented as a sinusoidal deformation with weak perturbations localized on the crests and troughs and no large oscillatory motions. This indicates the predominance of the plate's stabilizing forces over the external fluid forces. For $u_o > u_c$, a flutter instability appears and the resultant large-amplitude oscillations are a superposition of traveling and standing waves, whose decomposition can be obtained through two-dimensional Fourier transform or complex orthogonal decomposition [129]. This state presents a predictable f_o accompanied by higher-order harmonics. For this state, hydrodynamic pressure and viscous drag drive the locally stable plate out of equilibrium and into oscillatory motions. Finally, for $u_o > u_t > u_c$, where $u_t = 68.8$ ($\mathrm{Re}_t = 3.10 \times 10^5$), oscillations

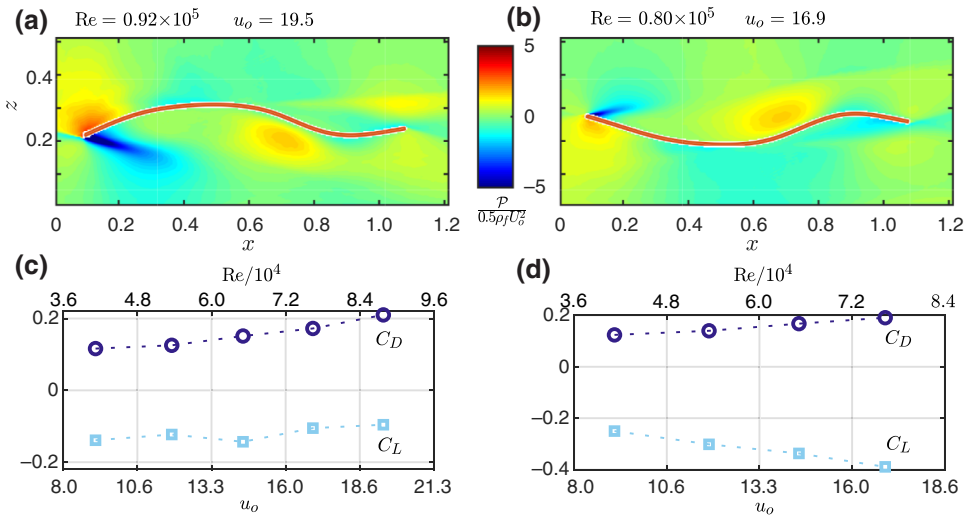

FIG. 5. Dimensionless pressure fields for the maximum upstream flow velocities for $u_o < u_c$ for the positive (a) and negative (b) phases. Dimensionless lift and drag coefficients for positive (c) and negative (d) phases [$C_D = F_D/(\frac{1}{2}L_p\rho_f U_o^2)$, $C_L = F_L/(\frac{1}{2}L_p\rho_f U_o^2)$, where F_d and F_l are the drag and lift forces per unit width acting on the plate].

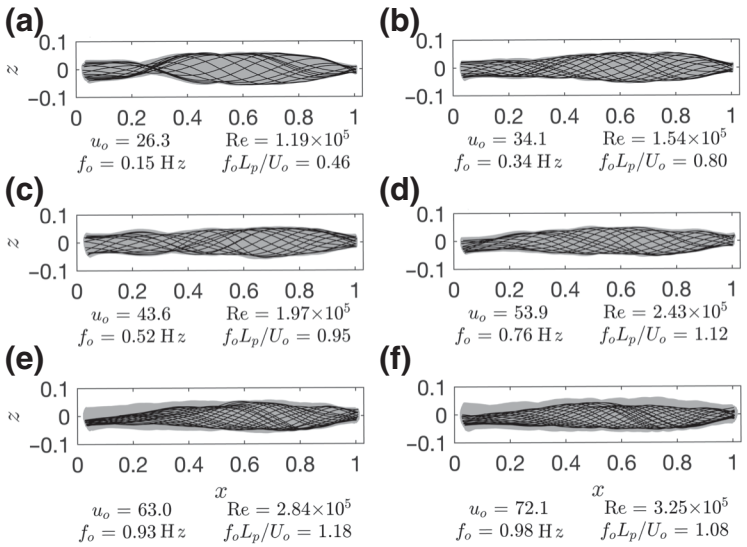

FIG. 6. Evolution of oscillatory motions over one period (T_o): ——, 15 plate locations equally spaced in time ($T_o/15$) over one oscillation period ($T_o = 1/f_o$); ■, envelope of maximum vertical excursions achieved in the test (350 s record sampled at 20 Hz). Flow direction is from left to right.

are characterized by a drop in the, to first order, linear trend of f_o, suggesting a transition from laminar to turbulent boundary layer on the plate (see Fig. 6 and accompanying videos in Supplemental Material for the three states of motion: *Flowregime1.mp4, Flowregime2.mp4*, and *Flowregime3.mp4* [82]). In this regime, the plate shows an increasingly broad subharmonic energy range in the spectra (i.e., precursor to chaos, Moon [130]), a loss of detectable higher harmonics, and an unstable limit cycle [Figs. 6(e) and 6(f)].

The plate under study also evinces an improved operational range with respect to flag or inverted flag configurations [33]. Experimental results show (see Fig. 2) that once u_c is exceeded, the plate oscillates with f_o proportional to u_o. As mentioned previously, this proportionality shows a drop at u_t. Subsequently, for $u_o > u_t$, f_o continues increasing at a somewhat flatter slope than that present for u_o in the range $u_c < u_o < u_t$. We note that u_o higher than 81.5 is not tested to preserve the physical integrity of the device.

IV. CONCLUDING REMARKS

We provide experimental evidence of the early onset of large oscillatory motions for a sinusoidally deformed flexible plate. We demonstrate that a lower u_c relative to either flag configuration can be achieved by the combination of three primary mechanisms: a deformed bistable plate, the destabilizing action of a net compressive force, and pressure drag. The start of large oscillatory motions in the proposed configuration occurs at $u_c = 26.6$, whereas experimental studies on flag-type configurations with similar fluid loading find $u_c = 197.0$ [83] and $u_c = 76.2$ [9].

First, by inducing an elastic instability through external compression, we force the device into a state of permanent deformation and local equilibrium, similar to the double-well restoring force potential of a bistable oscillator [29]. Thereafter, the plate is driven out of this state with the action of a small external force provided by a mean fluid flow and as a consequence a new locally stable deformed position is established. This is equivalent to the low-energy intrawell vibration exhibited by bistable devices [29]. The plate presents at least two physically realizable static deformations and, similar to a beam buckled by end loads, the geometric nonlinear stiffness is one of the causes of multiple equilibrium positions [130]. The other sources of nonlinearities for the proposed device are force boundary conditions [75]. Second, we present the destabilizing action of the net compressive force, which creates an early onset of oscillatory motions. The influence on u_c of increasing the net compressive force in a highly deformed plate should be the subject of a future investigation. Third, in the presence of a flow but before the plate oscillates (i.e., $u_o < u_c$), the sinusoidal deformation causes flow separation and therefore pressure drag increases as occurs on blunt bodies (e.g., cylinders [131]). A dominant form drag contribution is generated because of the difference between the high pressure at the frontal stagnation point and the low pressure in the rear separated region. This is analogous to the sinusoidally bent rigid body presented by Shelley and Zhang [28] [see their Figure 2(e)] and pitching airfoils [67,68]. The combined effects of a compressive force, a locally stable plate, and the unsteady flow field with non-negligible pressure drag and lift leads to the low u_c found in our experiments.

Furthermore, we demonstrate that subject to a fluid flow, the deformed plate evinces three states of motion: (a) a buckled plate with small perturbations for $u_o < u_c$, (b) a plate with large oscillatory motions appearing as a superposition of traveling and standing waves for $u_o > u_c$, showing predictable fundamental frequencies, and (c)

a plate with chaotic oscillatory motions for $u_o > u_t > u_c$, with a broad frequency spectrum but still predictable fundamental frequencies.

The plate configuration introduced herein, with its bistability, opens new possibilities for energy harvesting with a reduction of u_c and improved operational range when forced by fluid flow. Moreover, as occurs with flapping filaments or flags [22,132,133], the resemblance of the plate's induced oscillatory movements with animal locomotion poses the intriguing possibility of the deformed plate as a propulsion device or as a model to study locomotion itself. Work remains on the parametric exploration of compression and its influence on the onset of large oscillatory motions for highly deflected plates exhibiting mode 1 and mode 2 deformations and under the influence of turbulent incoming flows.

ACKNOWLEDGMENT

We thank B. Pietro Filardo for the concept and first device and Rafael O. Tinoco for the work related to the initial concept. This work was partially supported by the Atkinson Center for Sustainability, the DeFrees Fellowship at Cornell University, and the Colombian National Science Foundation, Colciencias.

APPENDIX A: EXPERIMENTAL STUDY CASES

Tables I–IV summarize the study cases using ADV, image-based point detection, image-based edge detection, and PIV, respectively.

1. Acoustic Doppler velocimetry

Velocity measurements (record lengths are 120 min) for all cases presented in Table I are performed with two Nortek Vectrino acoustic Doppler velocimeters with + firmware operating at 200 Hz, where one acoustic Doppler velocimeter is deployed $5L_p$ upstream of the plate's leading edge for U_o analysis, and the other $3L_p/4$ downstream from the leading edge to determine f_o. Data are analyzed with one-dimensional spectra.

2. Image-based point detection

For all cases presented in Table II, the plate's instantaneous location at 9 equispaced points in space are extracted with an image-based edge detection filter using images collected from a 480×480 pixel 14-bit CMOS sensor (Phantom V9.1). Record lengths are 33 min for the lowest flow velocity, and 20 min for the others, all at a sampling frequency of 18 Hz. Velocity measurements (record lengths of 30 min) are performed with two acoustic Doppler velocimeters with + firmware operating at 200 Hz, where one acoustic Doppler velocimeter is deployed $5L_p$ upstream of the plate's leading edge for U_o analysis, and the other $3L_p/4$ downstream from the leading edge to determine f_o.

TABLE I. Characterization of oscillatory frequency: experimental cases using acoustic Doppler velocimetry (ADV).

Test	U_o (cm/s)[a]	$\mathrm{Re}/10^5$	u_o
	Increasing upstream flow velocity		
01	19.7	1.18	26.2
02	21.9	1.31	29.1
03	25.6	1.54	34.7
04	29.1	1.75	38.7
05	32.9	1.97	43.8
06	36.7	2.20	48.8
07	40.4	2.43	53.8
08	43.9	2.63	58.4
09	47.4	2.84	63.1
10	51.0	3.06	67.9
11	54.7	3.28	72.8
12	58.4	3.51	78.4
13	61.8	3.71	82.2
	Decreasing upstream flow velocity		
14	62.2	3.73	82.8
15	59.2	3.55	78.8
16	55.9	3.36	74.4
17	52.3	3.14	69.6
18	48.9	2.93	65.1
19	45.3	2.72	60.3
20	41.8	2.51	55.6
21	37.0	2.22	49.2
22	33.2	1.99	44.2
23	29.6	1.78	39.4
24	26.2	1.57	34.9
25	22.9	1.37	30.5
26	20.6	1.24	27.4
27	18.9	1.13	25.1

[a]Maximum total error for upstream flow velocity, U_o, is ± 0.01 cm/s presented on test 27.

3. Image-based edge detection

For all cases presented in Table III, the plate's instantaneous geometry is extracted with an image-based edge

TABLE II. Characterization of the large oscillatory motion of a plate: experimental cases using image-based edge detection at a single point location.

Test	U_o (cm/s)[a]	$\mathrm{Re}/10^5$	u_o	Equispaced points
01	19.8	1.19	26.3	9
02	22.0	1.32	29.3	9
03	25.6	1.54	34.1	9
04	29.1	1.75	38.7	9
05	32.8	1.97	43.6	9
06	36.8	2.21	49.0	9

[a]Maximum total error for upstream flow velocity, U_o, is ± 0.01 cm/s presented on test 13.

TABLE III. Characterization of plate's large oscillatory motion: experimental cases using image-based edge detection.

Test	U_o (cm/s)[a]	Re/10^5	u_o
01	19.8	1.19	26.3
02	22.0	1.32	29.3
03	25.6	1.54	34.1
04	29.1	1.75	38.7
05	32.8	1.97	43.6
06	36.8	2.21	49.0
07	40.5	2.43	53.9
08	43.9	2.63	58.4
09	47.3	2.84	62.9
10	50.8	3.05	67.6
11	54.2	3.25	72.1
12	57.6	3.46	76.6
13	61.3	3.68	81.6

[a]Maximum total error for upstream flow velocity, U_o, is ± 0.01 cm/s presented on test 13.

TABLE IV. Characterization of the flow field: experimental cases using particle image velocimetry (PIV).

Test	U_o (cm/s)[a]	Re/10^5	$\triangle t$ (s)	Length (min)	u_o
01	6.9	0.44	0.0213	15	9.2
02[b]	6.9	0.44	0.0213	15	9.2
03	8.9	0.56	0.0165	15	11.8
04[b]	8.9	0.56	0.0165	15	11.8
05	10.8	0.68	0.0135	15	14.4
06[b]	10.9	0.69	0.0135	15	14.5
07	12.7	0.80	0.0114	15	16.9
08[b]	12.7	0.80	0.0114	15	16.9
09	14.6	0.92	0.0100	15	19.4
10[c]	16.7	1.05	0.0087	60	22.2
11	19.0	1.20	0.0076	60	25.3
12	28.8	1.81	0.0050	60	38.3
13	38.4	2.42	0.0038	60	51.1
14	48.0	3.02	0.0030	60	63.9
15	57.5	3.62	0.0025	60	76.5
16	61.2	3.85	0.0024	60	81.4

[a]Maximum total error for upstream flow velocity, U_o, is ± 0.01 cm/s presented on tests 3 and 16.
[b]Deformation of plate corresponds to the mirror over the x axis of the deformation of the previous test.
[c]Test corresponds to the critical velocity, U_c, which is the flow velocity at which large oscillatory motions start.

detection filter using images collected from a 1632×1200 pixel 14-bit CMOS sensor (Phantom V9.1). For the static deformation a single image per equilibrium position is used whereas for the large deformation cases 7000 images collected at 20 Hz are used per U_o. Velocity measurements (record lengths of 14 min) are performed with two acoustic Doppler velocimeters with + firmware at 200 Hz, where one acoustic Doppler velocimeter is deployed $5L_p$ upstream of the plate's leading edge for U_o analysis, and the other $3L_p/4$ downstream from the leading edge to determine f_o. Data is analyzed with one or two-dimensional spectra (2DFT), and complex orthogonal decomposition (COD, [129]).

4. Edge detection procedure

The general idea behind the detection algorithm is to smooth and reduce noise, enhance edge detection and find the plate's position with subpixel accuracy in the vertical coordinate. The procedure is as follows.

(1) Load image into a 16-bit unsigned integer format. This allows us to work in pixel coordinates and preserve the resolution of the original image.

(2) Perform a median filtering in two dimensions (3×3 neighborhood with zero padding at the edges) over the loaded data. This step reduces background noise. Zero padding skews the median near the image boundaries but does not affect the detection algorithm in the inner regions.

(3) Implement a Laplacian Gaussian filter (5×5 kernel with standard deviation of 0.2). This filter enhances edges and provides a clear limit between background noise and edge data. Here, the filter increases the intensity count of what is expected to be a surface edge to the maximum possible value (2^{16}).

(4) Apply a threshold filter. This step reduces the background noise that has been transformed into a white noise by the previous implementation of the Laplacian Gaussian filter, leaving at this point a mask that can be implemented over the original image.

(5) Multiply the original image by the mask. This step drives the intensity count to zero on pixels where there is no presence of edges.

(6) Apply a second round of the median filtering in two dimensions (3×3 neighborhood with zero padding at the edges). This filter is used to smooth and clean the residual noise.

(7) Determine the location of the maximum value of intensity count for every column (i.e., x coordinate). These data provide the z coordinate of the plate in pixel coordinates.

(8) Apply a median filter in one dimension (15th order). This filter is used to eliminate spurious points that could have entered during the detection of the pixel of maximum intensity.

(9) Apply a Gaussian fit at each x coordinate to seven pixels in the z coordinate in double precision format, and determine the location of the maximum value of the fit. These points include the pixel of maximum intensity, three above and three below in the z coordinate, providing a subpixel approximation for the location of the plate. As the Gaussian fit is overprescribed, the fitting method is nonlinear least squares.

(10) Apply a median filter in one dimension (15th order). This filter is used to eliminate spurious points that could have entered during the Gaussian fit.

APPENDIX B: UNCERTAINTY ANALYSIS

Unless otherwise stated, uncertainty associated with variables in the text is as follows.

1. Bias errors

The accuracy of the ADV is reported by the manufacturer as $\pm 0.5\%$ of the measured value or ± 1 mm/s, whichever is larger. To the former we add the error coming from misalignment on the experimental setup or probes in the wrong position owing to possible shocks during usage. This additional error will be accounted for as roll, pitch, and yaw movements, with an assumed maximum of 2° deviation angle, where only two out of the three rotations will be considered. If u_{real} is defined as $u_{\text{real}} = u_{\text{bias}}/\cos\theta$, the bias error due to roll movements is

$$\begin{aligned} \varepsilon &= u_{\text{real}} - u_{\text{bias}}, \\ \varepsilon &= u_{\text{real}} - u_{\text{real}}\cos\theta, \\ \varepsilon &= \frac{u_{\text{real}} - u_{\text{real}}\cos\theta}{u_{\text{real}}} = 1 - \cos\theta, \end{aligned} \tag{B1}$$

where the total error now considering a second rotation due only to misalignment is

$$\begin{aligned} \varepsilon &= \sqrt{(1-\cos\theta)^2 + (1-\cos\theta)^2}, \\ \varepsilon &= \sqrt{[1-\cos(2^\circ)]^2 + [1-\cos(2^\circ)]^2}, \\ \varepsilon &= 0.09\%, \end{aligned} \tag{B2}$$

and the total error, which is considered a bias error for velocity components or quantities with the same units as the velocity (e.g., turbulent intensity), is $\varepsilon = \sqrt{0.09\%^2 + 0.5\%^2} = 0.51\%$. The error for the Reynolds stress is considered as the square of this error. If the bias error calculated as 0.51% of the measured value is less than 1 mm/s or $(1\ \text{mm/s})^2$, the latter is chosen as the bias error.

For quantitative image-based edge and single point detection, the root-sum-squares technique [134] is considered for bias errors defined as $\delta R/R$:

$$\frac{\delta R}{R} = \left[\left(\frac{\partial L}{L}\right)_i^2 + \left(\frac{\partial T}{T}\right)_i^2\right]^{1/2}. \tag{B3}$$

Taking into account the errors of spatial calibration (1 per 1600 pixels), and camera trigger response time (1 μs per 0.005 s), for a maximum total bias error of $\varepsilon = 0.07\%$.

For PIV, as with image-based edge detection, the root-sum-squares [Eq. (B3)] technique is considered for the bias calculations, with errors of subwindow displacement (0.2 per 32 pixels, where 0.2 pixels is chosen as the subwindow displacement subpixel accuracy, see Cowen and Monismith [80]), spatial calibration (1 pixel per 2160 pixels), trigger response time (1 μs per 0.005 s), for a maximum total bias error of $\varepsilon = 0.63\%$.

2. Random error

The random error for both ADV and PIV is calculated based on the bootstrap analysis [135] with 1000 resamplings for the analysis of the statistic of interest, reporting the 95% confidence interval. The confidence interval band reported in all figures of spectral analysis has been done with this technique. The error reported in the edge detection results is the 95% confidence interval of the true error distribution (no bootstrap involved). For a full report of the maximum random absolute error bounds for velocity and turbulent metrics, and the 10%, 50%, and 90% percentile values of the relative error distribution bounds, see Muriel [77], where the latter values are chosen as typical metrics of these distributions.

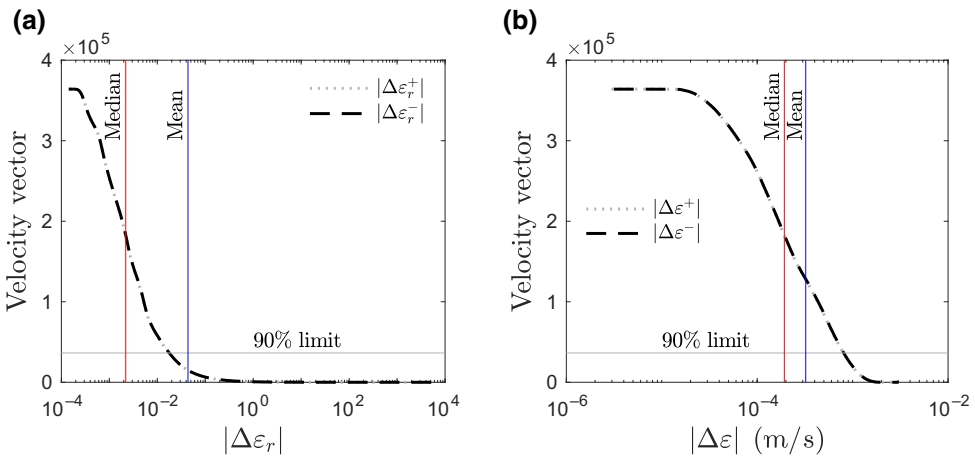

FIG. 7. Sorted relative (a) and absolute (b) random uncertainty bounds for the mean horizontal velocity, $\overline{u}$, containing all cases below critical flow velocity, u_c. Sorting of absolute and relative errors is independent, and (+) and (−) signs indicate upper and lower bounds, respectively.

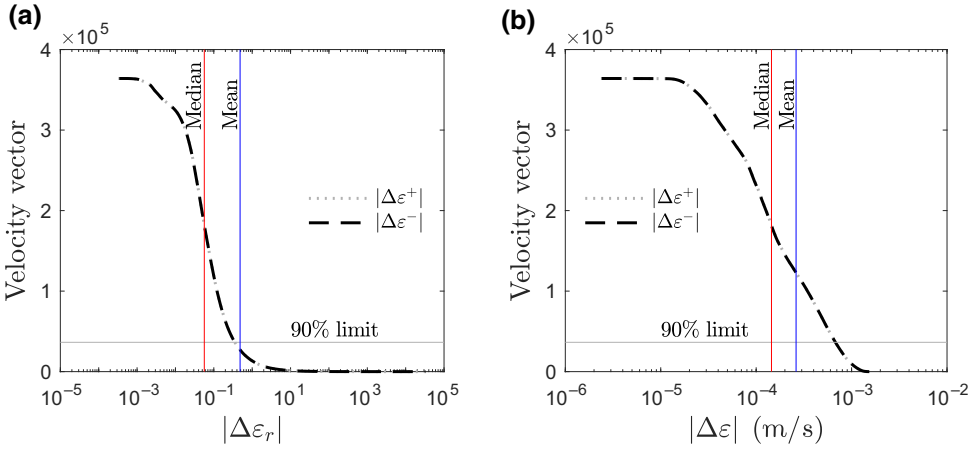

FIG. 8. Sorted relative (a) and absolute (b) random uncertainty bounds for the mean vertical velocity, $\overline{w}$, containing all cases below critical flow velocity, u_c. Sorting of absolute and relative errors is independent, and (+) and (−) signs indicate upper and lower bounds, respectively.

Special care is taken to report mean values of PIV for each variable of interest. We define absolute and relative errors as follows, taking the mean value of the horizontal velocity as an example ($\overline{u}$): the upper and lower error bounds are ε^+ and ε^-, respectively. These errors are the 95% confidence interval based on bootstrap analysis with 1000 resamplings. The upper and lower absolute error bounds are $\left|\Delta\varepsilon^+\right| = \left|\varepsilon^+ - \overline{u}\right|$, and $\left|\Delta\varepsilon^-\right| = \left|\varepsilon^- - \overline{u}\right|$, respectively. These errors have the units of the variables of interest. In addition, we report the dimensionless relative error, with upper and lower bounds defined as $\left|\Delta\varepsilon_r^+\right| = \left|\left(\varepsilon^+ - \overline{u}\right)/\overline{u}\right|$, and $\left|\Delta\varepsilon^-\right| = \left|\left(\varepsilon^- - \overline{u}\right)/\overline{u}\right|$, respectively.

We present the maximum absolute error ($|\Delta\varepsilon|$), and the 10%, 50%, and 90% percentile value of the relative error distribution ($|\Delta\varepsilon_r|$) per case. For example, the maximum $|\Delta\varepsilon|$ is the maximum of an $m \times n$ PIV grid. In a similar way, the percentile value intervals for $|\Delta\varepsilon_r|$ are the respective percentiles of the $m \times n$ PIV grid. This is presented to avoid misleading the reader towards the erroneous interpretation of the existence of high errors in the current dataset. Our experimental setup involves developing boundary layers, flow separation, and recirculation zones that drive time-averaged velocities and fluctuations close to, if not exactly to, zero. As expected, a relative error of such values grows inversely proportional to the mean value and, therefore, relative errors can appear excessively large.

Note, for example, how the value of the relative error grows to a considerably large value for $\overline{u}$ and $\overline{w}$, whereas the maximum absolute error remains low with respect to U_o (Figs. 7 and 8, respectively). These two distributions contain all velocity vectors for the static cases (i.e., all vectors contained in the $m \times n$ grids of the nine cases studied). An option here would be to simply normalize all values by U_o, but this option, as dividing by a small number, can be misleading as well, suggesting smaller uncertainties than in reality exist.

Tables V and VI present the maximum absolute and relative error for $u_o < u_c$.

3. Total error

With bias and random error defined, total error (ε_{tot}) can be determined by Eq. (B4)

$$\varepsilon_{\text{tot}} = \sqrt{\varepsilon_{\text{bias}}^2 + \varepsilon_{\text{random}}^2}. \tag{B4}$$

4. Other uncertainty

Additional uncertainty criteria are as follows.

(1) Uncertainty of single-sample data corresponds to half of the maximum resolution of the technique used to obtain the data point (i.e., data associated with length scales and oscillatory frequencies derived from one-dimensional spectral analysis).

(2) Confidence interval for small sample size determined as $\overline{x} \pm t_{df}^* s/\sqrt{n}$ [136] where $\overline{x}$ is the mean value, t_{df}^* is the value of Student's t-distribution with df degrees of freedom, s is the standard deviation, and n is the number of samples (i.e., plate thickness, δ, plate density, ρ_p, and tensile modulus, E).

TABLE V. Absolute ($|\Delta\varepsilon|$) error bounds for $u_o < u_c$. Absolute error is the maximum error.

	$\left\|\Delta\varepsilon^+\right\|$ (m/s)	$\left\|\Delta\varepsilon^-\right\|$ (m/s)
$\overline{u}$	0.0029	0.0031
$\overline{w}$	0.0017	0.0017
$\overline{u'}$	0.0019	0.0018
$\overline{w'}$	0.0012	0.0011
$\overline{u'w'}$	0.0001[a]	0.0001[a]

[a]Units are (m^2/s^2).

TABLE VI. Relative ($|\Delta\varepsilon_r|$) error bounds for $u_o < u_c$. Relative error is reported as a percentile of the distribution.

	Percentiles, reported as percentages.					
	10th		50th		90th	
	$\lvert\Delta\varepsilon_r^+\rvert$	$\lvert\Delta\varepsilon_r^-\rvert$	$\lvert\Delta\varepsilon_r^+\rvert$	$\lvert\Delta\varepsilon_r^-\rvert$	$\lvert\Delta\varepsilon_r^+\rvert$	$\lvert\Delta\varepsilon_r^-\rvert$
$\overline{u}$	0.05	0.05	0.22	0.23	1.78	1.78
$\overline{w}$	0.86	0.87	5.65	5.65	35.43	35.34
$\overline{u'}$	1.93	1.85	2.44	2.32	3.08	2.93
$\overline{w'}$	2.07	1.97	2.58	2.45	3.16	3.00
$\overline{u'w'}$	6.52	6.57	11.96	12.09	55.48	55.26

(3) Uncertainty for the transitional Reynolds number, Re_t, corresponds to half of the step change of u_o in f_o versus u_o trend, when Re_t occurs.

(4) Uncertainty for the reported hysteresis loop corresponds to maximum and minimum hysteresis loops considering the uncertainties associated to u_c.

5. Uncertainty associated with variables reported in the text

(1) Plate thickness: $\delta = 0.400 \pm 0.007$ mm.
(2) Plate length: $L_p = 60 \pm 0.05$ cm.
(3) Plate width: $B = 30 \pm 0.05$ cm.
(4) Plate density: $\rho_p = 1.14 \pm 0.03$ g/cm^3.
(5) Plate tensile modulus: $E = 1.97 \pm 0.04$ GPa.
(6) Tension-line length: $L_s = 7.62 \pm 0.05$ cm.
(7) Separation distance of tension-lines along the plate: $\delta_p = 2.90 \pm 0.05$ cm.
(8) Separation distance of tension-lines on the side-frame: $\delta_f = 2.45 \pm 0.05$ cm.
(9) Separation distance between side-frame lines: $B_r = 44.10 \pm 0.05$ cm.
(10) Mean positions of plate above the bottom of the recirculating flume: 15 ± 0.05 cm.
(11) Water depth: $h = 37 \pm 0.05$ cm.

[1] A. D. Lucey, The excitation of waves on a flexible panel in a uniform flow, Philos. Trans. A Math. Phys. Eng. Sci. **356**, 2999 (1998).
[2] R. K. Jaiman, E. Loth, and J. C. Dutton, Simulations of normal shock-wave/boundary-layer interaction control using mesoflaps, J. Propul. Power **20**, 344 (2004).
[3] L. Tang, M. P. Paidoussis, and J. Jiang, Cantilevered flexible plates in axial flow: Energy transfer and the concept of flutter-mill, J. Sound Vib. **326**, 263 (2009).
[4] J. J. Allen and A. J. Smits, Energy harvesting eel, J. Fluids Struct. **15**, 629 (2001).
[5] G. W. Taylor, J. R. Burns, S. M. Kammann, W. B. Powers, B. William, and T. R. Wel, The energy harvesting eel: A small subsurface ocean/river power generator, IEEE J. Ocean. Eng. **26**, 539 (2001).
[6] A. H. Techet, J. J. Allen, and A. J. Smits, in *The Twelfth International Offshore and Polar Engineering Conference* (International Society of Offshore and Polar Engineers, Kitakyushu, Japan, 2002), p. 713.
[7] H. D. Akaydin, N. Elvin, and Y. Andreopoulos, Wake of a cylinder: A paradigm for energy harvesting with piezoelectric materials, Exp. Fluids **49**, 291 (2010).
[8] S. Li, J. Yuan, and H. Lipson, Ambient wind energy harvesting using cross-flow fluttering, J. Appl. Phys. **109**, 026104 (2011).
[9] A. Giacomello and M. Porfiri, Underwater energy harvesting from a heavy flag hosting ionic polymer metal composites, J. Appl. Phys. **109**, 084903 (2011).
[10] J. A. Dunnmon, S. C. Stanton, B. P. Mann, and E. H. Dowell, Power extraction from aeroelastic limit cycle oscillations, J. Fluids Struct. **27**, 1182 (2011).
[11] R. K. Fancett and W. A. Clayden, Subsonic wind tunnel tests on the use of streamers to stabilize the FOIL bomblet, Tech. Rep. Memorandum 14/70 (Royal Armament Research and Development Establishment, 1972).
[12] L. Auman and B. Wilks, in *18th AIAA Aerodynamic Decelerator Systems Technology Conference and Seminar* (American Institute of Aeronautics and Astronautics, Munich, Germany, 2005), p. 1.
[13] L. Huang, Flutter of cantilevered plates in axial-flow, J. Fluids Struct. **9**, 127 (1995).
[14] T. S. Balint and A. D. Lucey, Instability of a cantilevered flexible plate in viscous channel flow, J. Fluids Struct. **20**, 893 (2005).
[15] R. M. Howell, A. D. Lucey, P. W. Carpenter, and M. W. Pitman, Interaction between a cantilevered-free flexible plate and ideal flow, J. Fluids Struct. **25**, 544 (2009).
[16] A. J. Fenlon and T. David, Numerical models for the simulation of flexible artificial heart valves: Part I-computational methods, Comput. Methods Biomech. Biomed. Eng. **4**, 323 (2001).
[17] A. J. Fenlon and T. David, Numerical models for the simulation of flexible artificial heart valves: Part II-valve studies, Comput. Methods Biomech. Biomed. Eng. **4**, 449 (2001).
[18] B. W. Smith, J. G. Chase, R. I. Nokes, G. M. Shaw, and G. Wake, Minimal haemodynamic system model including ventricular interaction and valve dynamics, Med. Eng. Phys. **26**, 131 (2004).
[19] G. Huber, Swimming in flatsea, Nature **408**, 777 (2000).
[20] M. S. Triantafyllou, G. S. Triantafyllou, and D. K. P. Yue, Hydrodynamics of fishlike swimming, Annu. Rev. Fluid Mech. **32**, 33 (2000).
[21] J. C. Liao, D. N. Beal, G. V. Lauder, and M. S. Triantafyllou, Fish exploiting vortices decrease muscle activity, Science **302**, 1566 (2003).
[22] U. K. Müller, Fish'n flag, Science **302**, 1511 (2003).
[23] Y. Watanabe, K. Isogai, S. Suzuki, and M. Sugihara, A theoretical study of paper flutter, J. Fluid Struct. **16**, 543 (2002).
[24] Y. Watanabe, S. Suzuki, M. Sugihara, and Y. Sueoka, An experimental study of paper flutter, J. Fluid Struct. **16**, 529 (2002).
[25] Y. B. Chang and P. M. Moretti, Flow-induced vibration of free edges of thin films, J. Fluids Struct. **16**, 989 (2002).

[26] J. K. Vandiver, Dimensionless parameters important to the prediction of vortex-induced vibration of long, flexible cylinders in ocean currents, J. Fluids Struct. **7**, 423 (1993).
[27] J. Zhang, S. Childress, A. Libchaber, and M. Shelley, Flexible filaments in a flowing soap film as a model for one-dimensional flags in a two-dimensional wind, Nature **408**, 835 (2000).
[28] M. J. Shelley and J. Zhang, Flapping and bending bodies interacting with fluid flows, Annu. Rev. Fluid Mech. **43**, 449 (2011).
[29] R. L. Harne and K. W. Wang, A review of the recent research on vibration energy harvesting via bistable systems, Smart Mater. Struct. **22**, 023001 (2013).
[30] L. Van Blarigan, P. Danzl, and J. Moehlis, A broadband vibrational energy harvester, Appl. Phys. Lett. **100**, 253904 (2012).
[31] S. M. Jung and K. S. Yun, Energy-harvesting device with mechanical frequency-up conversion mechanism for increased power efficiency and wideband operation, Appl. Phys. Lett. **96**, 111906 (2010).
[32] F. Cottone, L. Gammaitoni, H. Vocca, M. Ferrari, and V. Ferrari, Piezoelectric buckled beams for random vibration energy harvesting, Smart Mater. Struct. **21**, 035021 (2012).
[33] D. Kim, J. Cossé, C. H. Cerdeira, and M. Gharib, Flapping dynamics of an inverted flag, J. Fluid Mech. **736**, R1 (2013).
[34] J. Ryu, S. G. Park, B. Kim, and H. J. Sung, Flapping dynamics of an inverted flag in a uniform flow, J. Fluids Struct. **57**, 159 (2015).
[35] J. E. Sader, J. Cossé, D. Kim, B. Fan, and M. Gharib, Large-amplitude flapping of an inverted flag in a uniform steady flow—a vortex-induced vibration, J. Fluid Mech. **793**, 524 (2016).
[36] L. Golubovi cć, D. Moldovan, and A. Peredera, Dynamics of the Euler Buckling Instability, Phys. Rev. Lett. **81**, 3387 (1998).
[37] D. Bigoni, *Nonlinear Solid Mechanics: Bifurcation Theory and Material Instability* (Cambridge University Press, New York, 2012).
[38] E. H. Dowell, *Aeroelasticity of Plates and Shells* (Noordhoff International Publishing, Leyden, 1975), 1st ed.
[39] E. H. Dowell, *A Modern Course in Aeroelasticity* (Springer, Switzerland, 2015), 5th ed.
[40] E. H. Dowell and M. Ilgamov, *Studies in Nonlinear Aeroelasticity* (Springer-Verlag, New York, 1988).
[41] M. P. Paidoussis, *Fluid-Structure Interactions: Slender Structures and Axial Flow* (Academic Press, Oxford, 2016), 2nd ed., Vol. 1.
[42] M. P. Paidoussis, *Fluid-Structure Interactions: Slender Structures and Axial Flow* (Academic Press, Oxford, 2016), 2nd ed., Vol. 2.
[43] C. Topea, A. L. Yarin, and J. F. Foss, *Handbook of Experimental Fluid Mechanics* (Springer-Verlag, Berlin, 2007).
[44] L. Tang and M. P. Paidoussis, On the instability and the post-critical behaviour of two-dimensional cantilevered flexible plates in axial flow, J. Sound Vib. **305**, 97 (2007).
[45] C. Eloy, C. Souilliez, and L. Schouveiler, Flutter of a rectangular plate, J. Fluids Struct. **23**, 904 (2007).
[46] C. Eloy, R. Lagrange, C. Souilliez, and L. Schouveiler, Aeroelastic instability of cantilevered flexible plates in uniform flow, J. Fluid Mech. **611**, 97 (2008).
[47] S. Michelin, S. G. L. Smith, and B. J. Glover, Vortex shedding model of a flapping flag, J. Fluid Mech. **617**, 1 (2008).
[48] S. Alben and M. J. Shelley, Flapping States of a Flag in an Inviscid Fluid: Bistability and the Transition to Chaos, Phys. Rev. Lett. **100**, 074301 (2008).
[49] O. Doaré, M. Sauzade, and C. Eloy, Flutter of an elastic plate in a channel flow: Confinement and finite-size effects, J. Fluids Struct. **27**, 76 (2011).
[50] C. Eloy, N. Kofman, and L. Schouveiler, The origin of hysteresis in the flag instability, J. Fluid Mech. **691**, 583 (2012).
[51] L. Schouveiler and C. Eloy, in *Experimental and Theoretical Advances in Fluid Dynamics* (Springer, Berlin, Heidelberg, 2012), p. 3.
[52] B. Fan, C. Huertas-Cerdeira, J. Cossé, J. E. Sader, and M. Gharib, Effect of morphology on the large-amplitude flapping dynamics of an inverted flag in a uniform flow, J. Fluid Mech. **874**, 526 (2019).
[53] O. Doaré and S. Michelin, Piezoelectric coupling in energy-harvesting fluttering flexible plates: Linear stability analysis and conversion efficiency, J. Fluids Struct. **27**, 1357 (2011).
[54] D. T. Akcabay and Y. L. Young, Hydroelastic response and energy harvesting potential of flexible piezoelectric beams in viscous flow, Phys. Fluids **24**, 054106 (2012).
[55] K. Singh, S. Michelin, and E. De Langre, Energy harvesting from axial fluid-elastic instabilities of a cylinder, J. Fluids Struct. **30**, 159 (2012).
[56] K. Singh, S. Michelin, and E. De Langre, The effect of non-uniform damping on flutter in axial flow and energy-harvesting strategies, Philos. Trans. A Math. Phys. Eng. Sci. **468**, 3620 (2012).
[57] S. Michelin and O. Doaré, Energy harvesting efficiency of piezoelectric flags in axial flows, J. Fluid Mech. **714**, 489 (2013).
[58] Y. Xia, S. Michelin, and O. Doaré, Fluid-Solid-Electric Lock-in of Energy-Harvesting Piezoelectric Flags, Phys. Rev. Appl. **3**, 014009 (2015).
[59] J. Young, J. Lai, and M. F. Platzer, A review of progress and challenges in flapping foil power generation, Prog. Aerosp. Sci. **67**, 2 (2014).
[60] Q. Xiao and Q. Zhu, A review on flow energy harvesters based on flapping foils, J. Fluids Struct. **46**, 174 (2014).
[61] P. Ma, Z. Yang, Y. Wang, H. Liu, and Y. Xie, Energy extraction and hydrodynamic behavior analysis by an oscillating hydrofoil device, Renewable Energy **113**, 648 (2017).
[62] D. Kim, B. Strom, S. Mandre, and K. Breuer, Energy harvesting performance and flow structure of an oscillating hydrofoil with finite span, J. Fluids Struct. **70**, 314 (2017).
[63] M. Lahooti and D. Kim, Multi-body interaction effect on the energy harvesting performance of a flapping hydrofoil, Renewable Energy **130**, 460 (2019).
[64] T. Kinsey and G. Dumas, Parametric study of an oscillating airfoil in a power-extraction regime, AIAA J. **46**, 1318 (2008).

[65] J. Zhan, B. Xu, J. Wu, and J. Wu, Power extraction performance of a semi-activated flapping foil in gusty flow, J. Bionic Eng. **14**, 99 (2017).
[66] T. Kinsey, G. Dumas, G. Lalande, J. Ruel, A. Méhut, P. Viarouge, J. Lemay, and Y. Jean, Prototype testing of a hydrokinetic turbine based on oscillating hydrofoils, Renewable Energy **36**, 1710 (2011).
[67] K. Ramesh, J. Murua, and A. Gopalarathnam, Limit-cycle oscillations in unsteady flows dominated by intermittent leading-edge vortex shedding, J. Fluids Struct. **55**, 84 (2015).
[68] Y. Su, M. Miller, S. Mandre, and K. Breuer, Confinement effects on energy harvesting by a heaving and pitching hydrofoil, J. Fluids Struct. **84**, 233 (2019).
[69] J. Veilleux and G. Dumas, Numerical optimization of a fully-passive flapping-airfoil turbine, J. Fluids Struct. **70**, 102 (2017).
[70] E. M. H. Garcia and M. M. Bernitsas, Effect of damping on variable added mass and lift of circular cylinders in vortex-induced vibrations, J. Fluids Struct. **80**, 451 (2018).
[71] K. Raghavan and M. M. Bernitsas, Experimental investigation of reynolds number effect on vortex induced vibration of rigid circular cylinder on elastic supports, Ocean Eng. **38**, 719 (2011).
[72] H. A. Sodano, G. Park, and D. J. Inman, Estimation of electric charge output for piezoelectric energy harvesting, Strain **40**, 49 (2004).
[73] C. Souilliez, C. Eloy, and L. Schouveiler, in *ASME 2006 Pressure Vessels and Piping/ICPVT-11 Conference* (American Society of Mechanical Engineers, Vancouver, Canada, 2006), p. 465.
[74] D. F. Muriel, R. O. Tinoco, B. P. Filardo, and E. A. Cowen, Development of a novel, robust, sustainable and low cost self-powered water pump for use in free-flowing liquid streams, Renewable Energy **91**, 466 (2016).
[75] D. F. Muriel and E. A. Cowen, On the realization of a second buckling mode in a periodically-constrained heavy elastica, Extreme Mech. Lett. **21**, 76 (2018).
[76] S. Timoshenko and S. Woinowsky-Krieger, *Theory of Plates and Shells* (McGraw Hill, United States of America, 1987), 2nd ed.
[77] D. Muriel, Ph.D. thesis, Cornell University (2018).
[78] D. F. Muriel and E. A. Cowen, Uncertainty on pressure reconstruction through global integration of average velocity fields with immersed obstacles (to be published).
[79] L. Gui, S. T. Wereley, and Y. H. Kim, Advances and applications of the digital mask technique in particle image velocimetry experiments, Meas. Sci. Technol. **14**, 1820 (2003).
[80] E. A. Cowen and S. G. Monismith, A hybrid digital particle tracking velocimetry technique, Exp. Fluids **22**, 199 (1997).
[81] S. Wereley and C. Meinhart, Second-order accurate particle image velocimetry, Exp. Fluids **31**, 258 (2001).
[82] See Supplemental Material at http://link.aps.org/supplemental/10.1103/PhysRevApplied.13.014050 for videos.
[83] M. Shelley, N. Vandenberghe, and J. Zhang, Heavy Flags Undergo Spontaneous Oscillations in Flowing Water, Phys. Rev. Lett. **94**, 094302 (2005).
[84] M. Derakhshani and T. A. Berfield, Snap-through and mechanical strain analysis of a mems bistable vibration energy harvester, Shock Vib. **2019**, 6743676 (2019).
[85] E. H. Dowell, Nonlinear oscillations of a fluttering plate, AIAA J. **4**, 1267 (1966).
[86] E. H. Dowell, Nonlinear oscillations of a fluttering plate. II, AIAA J. **5**, 1856 (1967).
[87] E. H. Dowell, Flutter of buckled plates at zero dynamic pressure, AIAA J. **8**, 583 (1970).
[88] E. H. Dowell, Flutter of a buckled plate as an example of chaotic motion of a deterministic autonomous system, J. Sound Vib. **85**, 333 (1982).
[89] M. P. Paidoussis, Dynamics of flexible slender cylinders in axial flow part 1. Theory, J. Fluid Mech. **26**, 717 (1966).
[90] B. S. H. Connell and D. K. P. Yue, Flapping dynamics of a flag in a uniform stream, J. Fluid Mech. **581**, 33 (2007).
[91] S. Eskinazi, An investigation on fully developed turbulent flows in a curved channel, J. Aeronaut. Sci. **23**, 23 (1956).
[92] J. C. Rotta, Effect of streamwise wall curvature on compressible turbulent boundary layers, Phys. Fluids **10**, S174 (1967).
[93] R. Narasimha and S. K. Ojha, Effect of longitudinal surface curvature on boundary layers, J. Fluid Mech. **29**, 187 (1967).
[94] P. Bradshaw, The analogy between streamline curvature and buoyancy in turbulent shear flow, J. Fluid Mech. **36**, 177 (1969).
[95] R. M. C. So and G. L. Mellor, Experiment on convex curvature effects in turbulent boundary layers, J. Fluid Mech. **60**, 43 (1973).
[96] A. J. Smits, S. T. B. Young, and P. Bradshaw, The effect of short regions of high surface curvature on turbulent boundary layers, J. Fluid Mech. **94**, 209 (1979).
[97] R. L. Simpson, Y.-T. Chew, and B. G. Shivaprasad, The structure of a separating turbulent boundary layer. part 1. mean flow and reynolds stresses, J. Fluid Mech. **113**, 23 (1981).
[98] R. L. Simpson, Y.-T. Chew, and B. G. Shivaprasad, The structure of a separating turbulent boundary layer. Part 2. Higher-order turbulence results, J. Fluid Mech. **113**, 53 (1981).
[99] K. Shiloh, B. G. Shivaprasad, and R. L. Simpson, The structure of a separating turbulent boundary layer. Part 3. Transverse velocity measurements, J. Fluid Mech. **113**, 75 (1981).
[100] H. H. Fernholz and J.-D. Vagt, Turbulence measurements in an adverse-pressure-gradient three-dimensional turbulent boundary layer along a circular cylinder, J. Fluid Mech. **111**, 233 (1981).
[101] P. H. Hoffmann, K. C. Muck, and P. Bradshaw, The effect of concave surface curvature on turbulent boundary layers, J. Fluid Mech. **161**, 371 (1985).
[102] K. C. Muck, P. H. Hoffmann, and P. Bradshaw, The effect of convex surface curvature on turbulent boundary layers, J. Fluid Mech. **161**, 347 (1985).
[103] A. E. Alving, A. J. Smits, and J. H. Watmuff, Turbulent boundary layer relaxation from convex curvature, J. Fluid Mech. **211**, 529 (1990).

[104] P. R. Bandyopadhyay and A. Ahmed, Turbulent boundary layers subjected to multiple curvatures and pressure gradients, J. Fluid Mech. **246**, 503 (1993).
[105] B. Chebbi, A. G. L. Holloway, and S. Tavoularis, The response of sheared turbulence to changes in curvature, J. Fluid Mech. **358**, 223 (1998).
[106] A. G. L. Holloway, D. C. Roach, and H. Akbary, Combined effects of favourable pressure gradient and streamline curvature on uniformly sheared turbulence, J. Fluid Mech. **526**, 303 (2005).
[107] D. C. Roach and A. G. L. Holloway, Combined effects of flow curvature and rotation on uniformly sheared turbulence, J. Fluid Mech. **628**, 371 (2009).
[108] P. S. Jackson and J. C. R. Hunt, Turbulent wind flow over a low hill, Q. J. Roy. Meteor. Soc. **101**, 929 (1975).
[109] V. Baskaran, A. J. Smits, and P. N. Joubert, A turbulent flow over a curved hill part 1. Growth of an internal boundary layer, J. Fluid Mech. **182**, 47 (1987).
[110] V. Baskaran, A. J. Smits, and P. N. Joubert, A turbulent flow over a curved hill. Part 2. Effects of streamline curvature and streamwise pressure gradient, J. Fluid Mech. **232**, 377 (1991).
[111] S. E. Belcher and J. C. R. Hunt, Turbulent flow over hills and waves, Annu. Rev. Fluid Mech. **30**, 507 (1998).
[112] D. P. Zilker, G. W. Cook, and T. J. Hanratty, Influence of the amplitude of a solid wavy wall on a turbulent flow. Part 1. Non-separated flows, J. Fluid Mech. **82**, 29 (1977).
[113] J. Abrams and T. J. Hanratty, Relaxation effects observed for turbulent flow over a wavy surface, J. Fluid Mech. **151**, 443 (1985).
[114] K. A. Frederick and T. J. Hanratty, Velocity measurements for a turbulent nonseparated flow over solid waves, Exp. Fluids **6**, 477 (1988).
[115] D. P. Zilker and T. J. Hanratty, Influence of the amplitude of a solid wavy wall on a turbulent flow. Part 2. Separated flows, J. Fluid Mech. **90**, 257 (1979).
[116] J. D. Kuzan, T. J. Hanratty, and R. J. Adrian, Turbulent flows with incipient separation over solid waves, Exp. Fluids **7**, 88 (1989).
[117] J. D. Hudson, L. Dykhno, and T. J. Hanratty, Turbulence production in flow over a wavy wall, Exp. Fluids **20**, 257 (1996).
[118] J. Buckles, T. J. Hanratty, and R. J. Adrian, Turbulent flow over large-amplitude wavy surfaces, J. Fluid Mech. **140**, 27 (1984).
[119] M. Jayaram, M. W. Taylor, and A. J. Smits, The response of a compressible turbulent boundary layer to short regions of concave surface curvature, J. Fluid Mech. **175**, 343 (1987).
[120] P. Rojratsirikul, Z. Wang, and I. Gursul, Unsteady fluid–structure interactions of membrane airfoils at low reynolds numbers, Exp. Fluids **46**, 859 (2009).
[121] R. Gordnier, High fidelity computational simulation of a membrane wing airfoil, J. Fluid Struct. **25**, 897 (2009).
[122] P. Rojratsirikul, Z. Wang, and I. Gursul, Effect of prestrain and excess length on unsteady fluid-structure interactions of membrane airfoils, J. Fluid Struct. **26**, 359 (2010).
[123] M. Molki and K. Breuer, Oscillatory motions of a prestrained compliant membrane caused by fluid–membrane interaction, J. Fluid Struct. **26**, 339 (2010).
[124] P. Rojratsirikul, M. Genc, Z. Wang, and I. Gursul, Flow-induced vibrations of low aspect ratio rectangular membrane wings, J. Fluid Struct. **27**, 1296 (2011).
[125] J. W. Jaworski and R. E. Gordnier, High-order simulations of low reynolds number membrane airfoils under prescribed motion, J. Fluid Struct. **31**, 49 (2012).
[126] M. S. Genc, Unsteady aerodynamics and flow-induced vibrations of a low aspect ratio rectangular membrane wing with excess length, Exp. Therm. Fluid Sci. **44**, 749 (2013).
[127] R. E. Gordnier and P. J. Attar, Impact of flexibility on the aerodynamics of an aspect ratio two membrane wing, J. Fluid Struct. **45**, 138 (2014).
[128] L. Shen, X. Zhang, D. K. P. Yue, and M. S. Triantafyllou, Turbulent flow over a flexible wall undergoing a streamwise travelling wave motion, J. Fluid Mech. **484**, 197 (2003).
[129] B. F. Feeny, A complex orthogonal decomposition for wave motion analysis, J. Sound Vib. **310**, 77 (2008).
[130] F. C. Moon, *Chaotic and Fractal Dynamics: An Introduction for Applied Scientists and Engineers* (Wiley-VCH, Germany, 2004).
[131] C. H. K. Williamson, Vortex dynamics in the cylinder wake, Annu. Rev. of Fluid Mech. **28**, 477 (1996).
[132] L. B. Jia and X. Z. Yin, Passive Oscillations of two Tandem Flexible Filaments in a Flowing Soap Film, Phys. Rev. Lett. **100**, 228104 (2008).
[133] L. Ristroph and J. Zhang, Anomalous Hydrodynamic Drafting of Interacting Flapping Flags, Phys. Rev. Lett. **101**, 194502 (2008).
[134] S. J. Kline and F. A. McClintock, Describing uncertainties in single-sample experiments, ASME Mech. Eng. **75**, 3 (1953).
[135] B. Efron and R. J. Tibshirani, *An Introduction to the Bootstrap* (CRC press, Boca Raton, USA, 1994).
[136] J. L. Devore, *Probability and Statistics for Engineering and the Sciences* (Cengage Learning, Boston, USA, 2016), 9th ed.